Chapter 8

Performance

In this chapter we discuss the basic performance of the ALICE detector for track finding and reconstruction, charged particle identification and neutral particle detection as expected from Monte Carlo simulations. For a comprehensive review of the physics performance we refer the reader to [20, 21].

The ALICE detector was designed to cope with the highest predicted charged-particle multiplicity densities for central Pb-Pb collisions at LHC ($\mathrm{d}N_{\mathrm{ch}}/\mathrm{d}\eta$ at mid-rapidity up to 8000; see section 1.3.1 of [20]). In addition, the ALICE experiment will also study collisions of lower-mass ions, as a means of varying the energy density, and of protons (both pp and pA). Besides primarily providing a reference for the study of nucleus-nucleus interactions, pp data will also allow for a number of genuine pp-physics studies.

One of the most challenging tasks for ALICE is that of track finding in an unprecedented particle multiplicity density environment. Track finding begins with the reconstruction of the primary vertex using the correlation of the hit positions in the innermost detector (SPD). The position of the primary vertex is then used as a constraint to initiate the tracking of primary particles in the TPC and for the subsequent track following. Secondary tracks are found during a further tracking pass. Finally, the reconstruction of secondary vertices is carried out.

Charged hadrons are identified combining information provided by the ITS, TPC, TRD, TOF, and HMPID detectors. Electrons are identified using information from the TRD and the TPC. The information from the EMCal will improve the purity of electron identification, especially at higher momenta. The PHOS spectrometer detects and identifies photons. Below about 20 GeV/c the direct-photon spectrum is obtained by subtracting, from the overall identified-photon spectrum, the contribution from decay photons, mainly from π^0, η, and ω decays. The yields of these mesons are measured by an invariant-mass analysis. At higher momenta, up to about 100 GeV/c, direct photons are identified on an event-by-event basis. The EMCal will enlarge the photon-identification acceptance, albeit with a performance not as high as that of the PHOS. In the forward pseudo-rapidity region ($2.3 < \eta < 3.5$) the photon multiplicity is measured by the PMD.

In the forward muon spectrometer, tracks are reconstructed behind the absorber, starting from the last stations and proceeding towards the interaction point. In this way we identify muons in the pseudo-rapidity region $-4.0 < \eta < -2.5$.

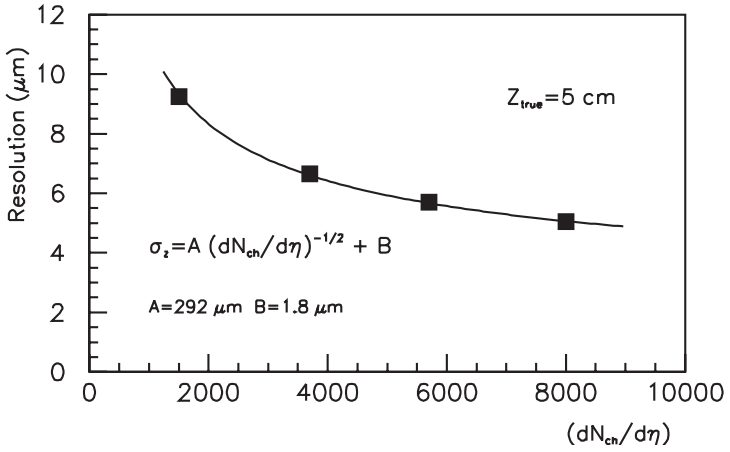

Figure 8.1: Resolution of the reconstructed vertex position as a function of the charged-particle density. The solid line is the result of a fit using the parametrization given by eq. (8.1).

8.1 Track and vertex reconstruction

8.1.1 Primary vertex determination

The reconstruction of the primary vertex is based on the information provided by the Silicon Pixel Detectors (SPD), which constitute the two innermost layers of the ITS. We select pairs of reconstructed points in the two layers, which are close in azimuthal angle in the transverse plane. Then from their z-coordinates we estimate the z-position of the primary vertex using a linear extrapolation. Finally we perform a similar procedure in the transverse plane. Here, due to the bending in the magnetic field, the linear extrapolation is a somewhat crude approximation; however, thanks to the short distances from the interaction point, the x- and y-coordinates of the primary vertex are determined with a sufficient precision to be used as constraints in the first tracking pass. This estimate of the primary vertex position is then used to correct the measurement of the z-coordinate, for effects due to an off-axis position of the interaction point in the transverse plane. For well focused beams we can determine the transverse position of the interaction point averaging over many events, provided that the beam position is sufficiently stable in time.

The resolution on the position of the primary vertex depends on the track multiplicity, i.e. on the charged-particle density. In figure 8.1 this dependence is shown for the resolution in the z-coordinate σ_z and is fitted by the expression

$$\sigma_z = \frac{A}{\sqrt{\mathrm{d}N_{\mathrm{ch}}/\mathrm{d}\eta}} + B, \tag{8.1}$$

where typically $A = 290\,\mu$m and B is a few microns, depending essentially on the residual misalignment of the silicon pixel layers. For heavy-ion charged-particle densities we thus obtain a vertex-position resolution on the $10\,\mu$m level, and for the average pp event ($\mathrm{d}N_{\mathrm{ch}}/\mathrm{d}\eta = 6$–$7$) we get $150\,\mu$m. This measurement of the primary-vertex position is used as an input for the tracking.

After track reconstruction, the position of the primary vertex is recalculated using the measured track parameters. In figure 8.2 the expected final resolutions in the z-coordinate, and in the

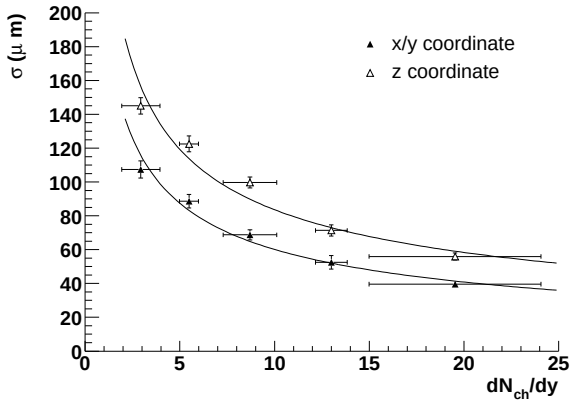

Figure 8.2: Resolution on the primary-vertex position as determined using reconstructed tracks, as a function of the charged-particle density for pp events.

transverse x/y-coordinates, are shown as a function of the charged-particle density (for pp collisions). When fitting these dependencies to eq. (8.1) we get $A = 270\,\mu$m for the z-coordinate, and $A = 210\,\mu$m for the x/y-coordinate (again with a few microns for B). For the average pp multiplicity, the precision on the measurement of the primary vertex position after the tracking step is improved to $110\,\mu$m in the z-coordinate, and to $70\,\mu$m in the transverse coordinate.

8.1.2 Track reconstruction

The basic method employed for track finding and fitting is the Kalman filter as introduced to this field by P. Billoir [252]. This method depends critically on the determination, for each track, of a set of initial seed values for the track parameters and their covariance matrix. This seeding is done using the space points reconstructed in the TPC. The space-point positions are calculated from the centre of gravity of the two-dimensional clusters (in the pad-row and time directions). At high particle densities, due to the large occupancy, we use a more sophisticated cluster unfolding which takes into account the cluster structure. The seeding is done twice: the first time assuming that the track originated from the primary vertex and the second assuming that the track originated elsewhere (decay, secondary interaction, etc.). We start to combine the space points from a few outermost pad rows using, in the first pass, the primary-vertex position as a constraint. The procedure is repeated several times, choosing a set of pad rows closer and closer to the centre of the TPC. From every seed we start the track following, pad row by pad row inside the TPC. The Kalman filter essentially consists of the following steps: a) we propagate the state vector of the track parameters and their covariance matrix to the next pad row, b) we add to the inverted covariance matrix (which represents the information matrix of our knowledge of the track parameters at that point) a noise term (representing the information loss due to stochastic processes like multiple scattering and energy-loss fluctuations), c) if the filter finds in the new pad row a space point compatible with the track prolongation, we add this measurement, i.e. we update the track parameters and the covariance matrix, increasing the information. We repeat the seeding a second time, now without the primary-vertex constraint. We then proceed again with track following as outlined above. The track-finding

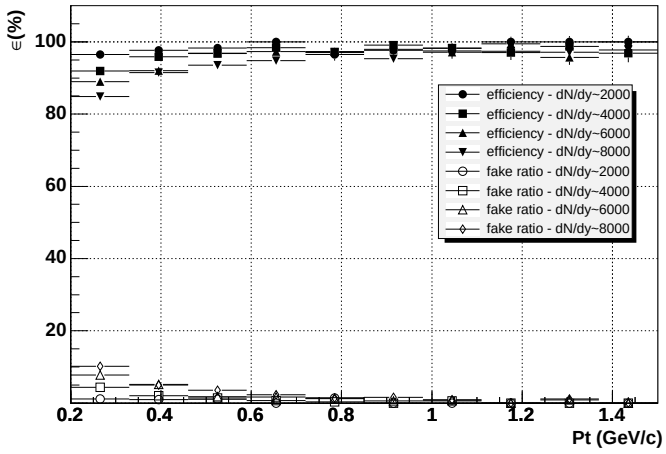

Figure 8.3: TPC and ITS track-finding efficiency and fraction of fake tracks as a function of transverse momentum for different track multiplicities.

efficiency after this stage, if we normalize to the number of tracks which are potentially findable (i.e. without taking into account decays in flight, detector acceptances, etc.) is nearly 100%.

After this step, the tracks are propagated to the outer layers of the ITS. We start with the highest-momentum tracks and then continue with the lower-momentum ones in order to make the most precise (i.e. less ambiguous) track-space point assignments first. For highly ionizing tracks in the TPC, this knowledge is used in the ITS tracking for energy-loss corrections and multiple-scattering noise estimates. Tracks found in the TPC as primaries are followed by the Kalman filter in two independent passes, first imposing the primary-vertex position as a constraint, and then without this condition. Both sets of track parameters are stored for further analysis. The tracks found during the second TPC pass (i.e. without vertex constraint) are followed in the ITS only without imposing the primary-vertex constraint. Whenever more than one space-point candidate is found within the search window around the prolongation of a track (a half-width of four standard deviations is typically used), all possible assignments are used as different hypotheses and are followed independently towards the innermost ITS layer. In this way each TPC track can have several candidate paths throughout the ITS. A decision is made only at the end, based on the sum of the χ^2 along the track-candidates' path in the ITS. Optionally, we allow for layer skipping and cluster sharing between tracks, in which case a weight factor is introduced in the χ^2 sum. The results for the combined TPC-ITS tracking are shown in figures 8.3 and 8.4. In figure 8.3 the expected track-finding efficiency for primary tracks and the relative frequency of fake tracks are presented as a function of transverse momentum for different charged-particle densities. The efficiency for primary tracks is normalized to the number of tracks which are potentially findable. Fake tracks are defined here as tracks that have more than one space point incorrectly assigned. For very high densities ($\mathrm{d}N_{\mathrm{ch}}/\mathrm{d}\eta = 6000$, well above the current theoretical predictions), the efficiency for tracks with $p_{\mathrm{t}} = 200$–$300\,\mathrm{MeV}/c$ is about 90%, and increases to values above 95% at higher momenta. The fake-track probability at the same time is below 10% in the lower momentum bin, and decreases below 1% at high momenta. For the same value of the charged-particle density figure 8.4 shows the expected quality of the TPC-ITS track finding, for different definitions of properly found and of fake tracks.

2008 JINST 3 S08002

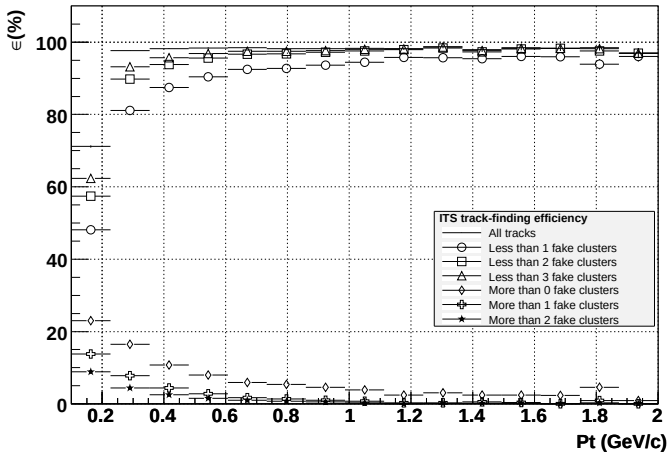

Figure 8.4: TPC and ITS track-finding efficiency and fraction of fake tracks for different amounts of wrongly associated ITS clusters ($\mathrm{d}N_{\mathrm{ch}}/\mathrm{d}\eta = 6000$).

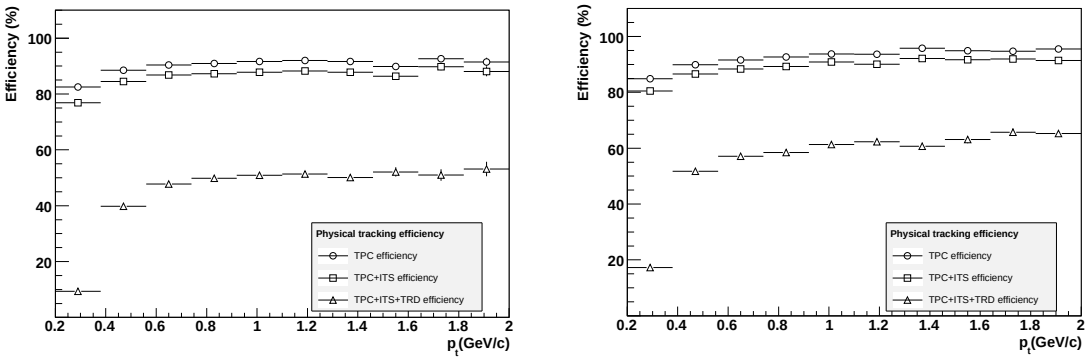

Figure 8.5: Physical track-finding efficiency for different combinations of the tracking detectors. Left: Central Pb–Pb collisions ($\mathrm{d}N_{\mathrm{ch}}/\mathrm{d}\eta = 6000$). Right: pp collisions.

When the ITS tracking is completed, we reverse the Kalman filter and follow the track from the inner ITS layers outwards. Starting with much more precise track parameters than during the first step, we now try to eliminate improperly assigned points (outliers). We then continue following the tracks beyond the TPC, assigning space points in the TRD, and matching the tracks with hits in the TOF, minimum-ionizing clusters in the HMPID and space points in the CPV (located in front of the PHOS). Finally, we reverse the Kalman filter one last time and we refit all tracks from the outside inwards, in order to obtain the values of the track parameters at or nearby the primary vertex. Optionally, we proceed with an additional track-finding step using only points from the ITS, after having removed all the ITS space points already assigned to tracks. This is useful for finding tracks that have not been seeded in the TPC because they went through a non-sensitive area (e.g. in between the readout chambers).

In figure 8.5 the track-finding efficiencies at different stages, this time normalized to the total number of primary charged tracks in the acceptance (i.e. taking into account decays and insensitive areas in the detectors) are presented as a function of transverse momentum, again for high

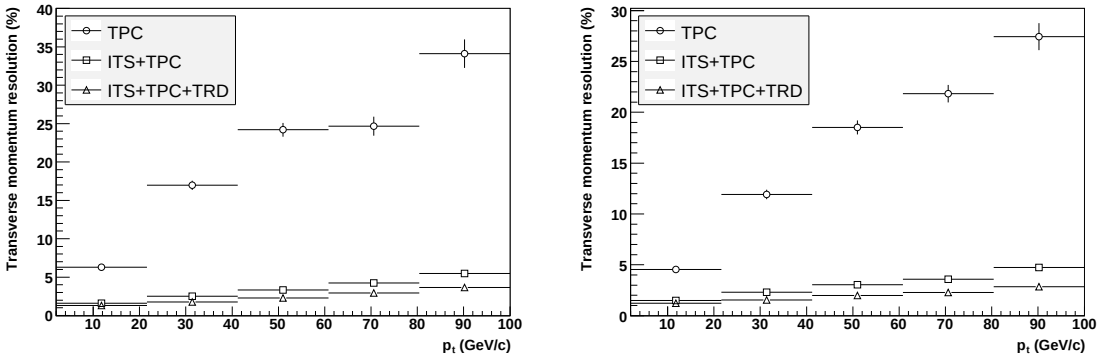

Figure 8.6: Transverse-momentum resolution for different combinations of the tracking detectors. Left: Central Pb–Pb collisions ($\mathrm{d}N_{\mathrm{ch}}/\mathrm{d}\eta = 6000$). Right: pp collisions.

charged-particle density ($\mathrm{d}N_{\mathrm{ch}}/\mathrm{d}\eta = 6000$) and for pp collisions. The efficiency for the TPC and the TPC-ITS track finding goes to 90% at very high momenta; this value is essentially determined by the size of the TPC dead zones, which cover about 10% of the azimuthal angle. The large drop after inclusion of the TRD is because of interactions in the material and decays as well as additional dead zones. The TRD, therefore, is used in the tracking optionally, only for those tracks for which it improves the precision. Figure 8.6 shows the momentum precision obtained with different detector combinations, again for two different values of the charged-particle density. The relative momentum precision for the TPC stand-alone shown in figure 8.6 is calculated without imposing the primary-vertex constraint. The significant improvement at high transverse momenta when we combine the measurements from the TPC and ITS is basically due to the increase in tracking length. The best relative momentum precision, limited by multiple scattering to about 0.7%, is achieved for low-momentum tracks with p_{t} about 500 MeV/c. For both the track-finding efficiency and the momentum precision, only a slight deterioration is seen when going from low to high charged-particle density.

The track parameters obtained both with and without the primary-vertex constraint are stored for all tracks, in order to allow for the subsequent analysis of short-lived particle decays (such as charm and beauty decays) taking place very close to the primary vertex. The main performance parameter for such studies is the resolution in the impact-parameter (the distance between the primary vertex and the track prolongation to the point of closest approach to the primary vertex). This resolution depends both on the precision of the primary-vertex-position determination and on the precision of the determination of the track-parameters. In figure 8.7 the impact-parameter resolution in the transverse and longitudinal directions is shown for different particle species as a function of p_{t}. These results were obtained for the case of central Pb-Pb collisions (i.e. with very high precision on the primary-vertex position). Figure 8.8 shows the impact-parameter resolution expected for two values of the charged-particle multiplicity in pp collisions (only for pions, and in the transverse direction). In all cases the impact-parameter resolution in the transverse direction (the quantity we rely upon for heavy-flavour physics) is significantly better than 100 μm at $p_{\mathrm{t}} \sim$ 1 GeV/c, a necessary condition to study e.g. charm decays.

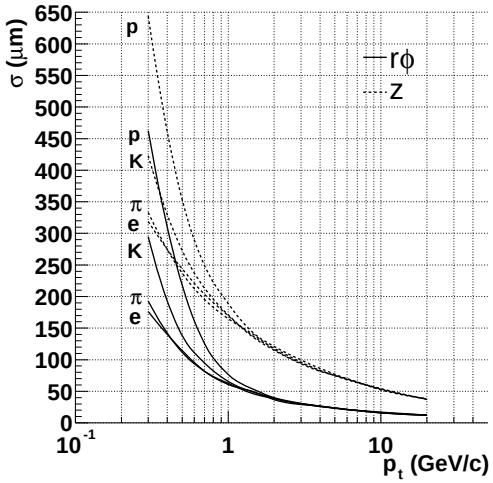

Figure 8.7: Impact parameter resolutions in central Pb-Pb collisions for electrons, pions, kaons and protons as a function of the transverse momentum. An assigned cluster in each of the six ITS layers is required.

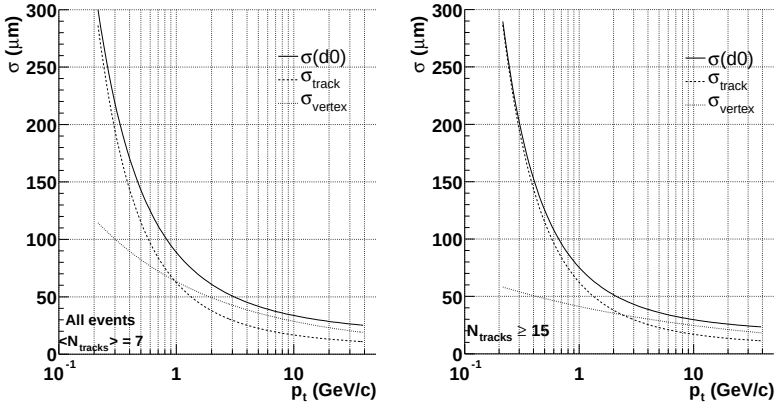

Figure 8.8: Impact-parameter resolution in the transverse plane as a function of the transverse momentum in pp collisions. The dotted lines show separately the contributions from the track extrapolation and the primary vertex accuracy.

8.1.3 Secondary-vertex finding

Vertices from strange particle decays are searched for at the reconstruction level. Only secondary tracks, i.e. tracks which have a large enough impact parameter, are used for this purpose. We combine opposite-sign secondary tracks and calculate their distance of closest approach. If this distance is below some predetermined value, and the point of the closest approach is located before the first measured points on both tracks, we retain the pair as a candidate for a secondary decay vertex. Additional cuts are then imposed in the subsequent analysis phase. An example of such an analysis is shown in figure 8.9 where the invariant mass distribution of $\Lambda \rightarrow \pi^{-}\mathrm{p}$ decay candidates is plotted. Tight cuts were applied on the distance of closest approach and on the pointing angle (the angle between reconstructed Λ momentum and the line joining the primary and secondary vertices), in order to maximize the signal-to-background ratio.

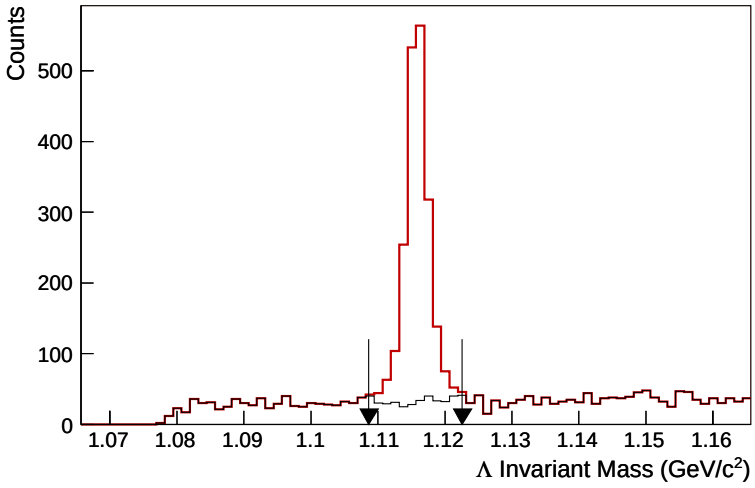

Figure 8.9: Λ invariant-mass spectrum corresponding to the reconstruction of 300 HIJING events ($\mathrm{d}N_{\mathrm{ch}}/\mathrm{d}\eta = 6000$), using tight cuts on the distance of closest approach and the pointing angle.

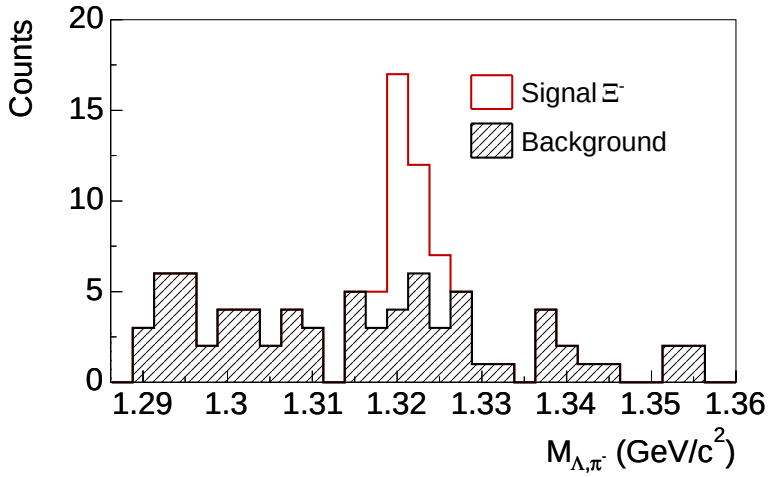

Figure 8.10: Ξ invariant mass spectrum obtained with the reconstruction of 300 HIJING events ($\mathrm{d}N_{\mathrm{ch}}/\mathrm{d}\eta = 6000$).

The selection on the value of the pointing angle is relaxed during the cascade reconstruction, in order not to bias the sample against cascade decays. As an example, we show in figure 8.10 the effective-mass plot obtained at the analysis level by combining reconstructed Λ candidates with a pion track to form another secondary vertex. A Ξ^- signal is clearly visible. Such a Λ would not in general point towards the primary vertex (the parent Ξ^- would).

At the reconstruction level, we also search for decays in flight within the TPC fiducial volume by combining a primary track disappearing before the end of the TPC, with a secondary track of the same sign. The track pair has to be closely matched in space and to have correct space ordering of the last measured point on the primary track and the first measured point on the secondary track. The efficiency for track finding for such decays is presented in figure 8.11 as a function of the radial position of the decay point in the TPC. The fiducial region to study charged-kaon and -pion decays is $120 < r < 210\,\mathrm{cm}$.

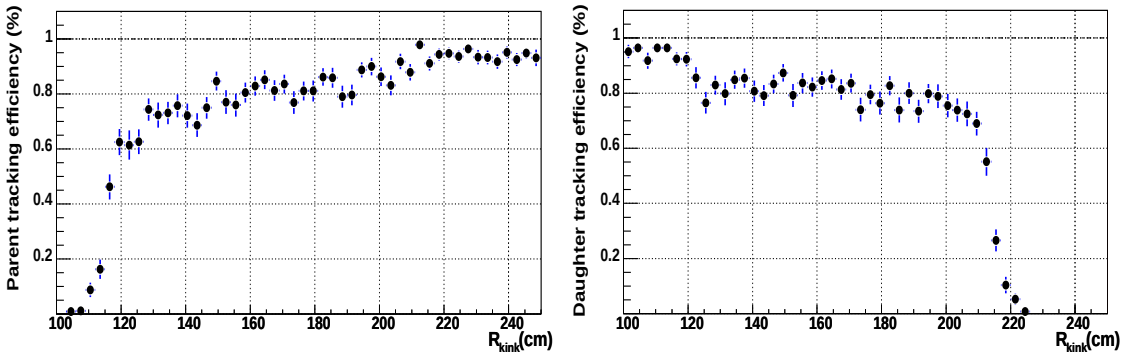

Figure 8.11: Left: Tracking efficiency for parent tracks as a function of the radial coordinate of the decay vertex. Right: Tracking efficiency for daughter tracks as a function of the radial coordinate of the decay vertex.

No attempt to reconstruct secondary vertices from decays of heavy-flavour particles is made at the reconstruction stage. Such decays are only dealt with at the analysis stage.

8.2 Particle identification

8.2.1 Charged-hadron identification

Several detectors, the ITS, TPC, TRD, TOF and HMPID, participate in the charged-Particle IDentification (PID), each with a different momentum-dependent performance. The best results are achieved by combining the information they provide individually. Particle identification is performed in two steps: during the first step, the information from each detector is used to assign to every track a set of probabilities, one for each particle type. The sum of these probabilities is normalized to unity. For example, if a detector has no identification power for a given track, it assigns equal probabilities to all particle types. On the other hand, if the detector unambiguously decides that the track is of a given type, it assigns probability 1 to that type, and 0 to the others. The procedure for combined PID must guarantee that, in the first of these two extreme cases (no identification power) the detector in question does not influence the result, and in the second (an unambiguous identification) the decision of the detector in question is final and cannot be altered by the information from other detectors. The information from the individual detectors is then combined in the second PID step, described later in the section.

Four layers of the ITS (two silicon-drift and two silicon-strip detector layers) provide signal-amplitude information, which can be used for PID in the low-momentum range by measuring ionization energy loss $\mathrm{d}E/\mathrm{d}x$. This is estimated as a truncated mean (using the two or three lowest amplitude signals out of four) in order to minimize the influence of Landau fluctuations. The resulting correlation plot is shown in figure 8.12. The resolution of the ITS $\mathrm{d}E/\mathrm{d}x$ measurement is about 11%, which allows for good π/K separation up to 450 MeV/c and for good p/K separation up to about 1 GeV/c. A typical ITS response function, for the momentum bin 400–425 MeV/c, is shown in figure 8.13. The tails at lower $\mathrm{d}E/\mathrm{d}x$ values for kaons and protons are due to the incorrect assignment of a cluster during track reconstruction. Such a cluster is with the largest probability

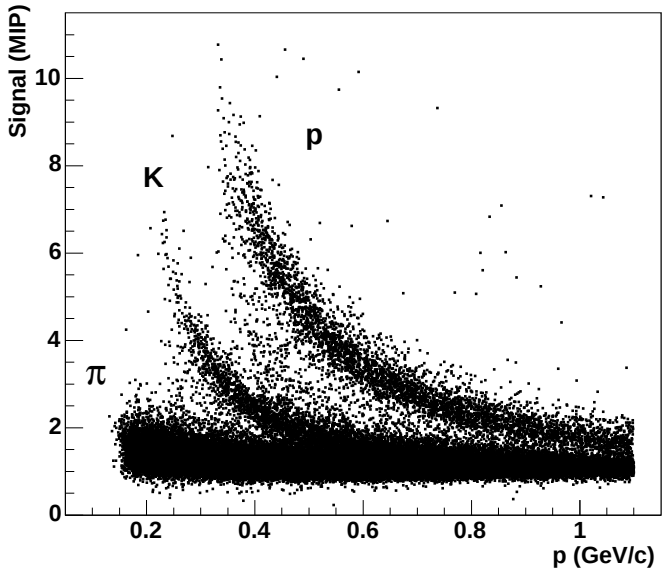

Figure 8.12: Plot of the correlation between the specific SDD/SSD signals (MIP units) calculated by the truncated mean method and the particle's momentum obtained from the TPC and ITS tracking for different particle species.

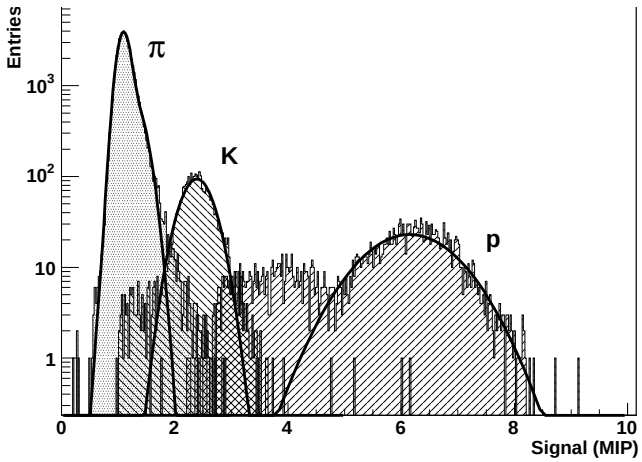

Figure 8.13: Distributions of the truncated mean SDD and SSD signals (MIP units) obtained with the HIJING generator for pions, kaons and protons for a reconstructed momentum of 400–425 MeV/c. The curves are the result of Gaussian approximations.

due to a pion, therefore lowering the truncated mean amplitude. The size of this effect will depend on the track-quality selection criteria which will have to be optimized on the real data sample and on the experimental particle-species ratios. The track probabilities for different particle types are calculated using such detector response functions.

The $\mathrm{d}E/\mathrm{d}x$ measurement in the TPC is treated in a similar way, using the truncated mean of the 65% lowest-amplitude pad-row samples. The estimated resolution of the $\mathrm{d}E/\mathrm{d}x$ measurement depends slightly on the charged-particle density; it changes from 5.5% for pp events to 6.5% for central Pb-Pb collisions. The simulated response function in the latter case is shown in figure 8.14

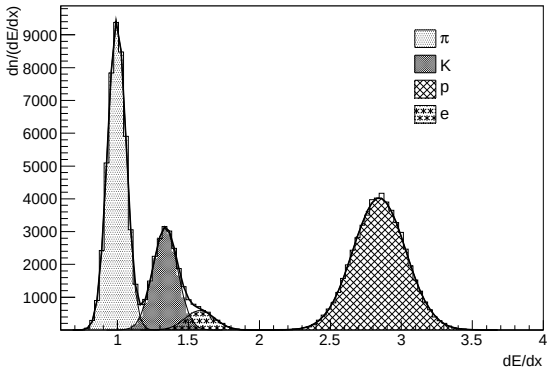

Figure 8.14: Simulated TPC $\mathrm{d}E/\mathrm{d}x$ distribution for electrons, pions, kaons, and protons with $p = 0.5\,\mathrm{GeV}/c$. The solid line indicates the result of the fit to a sum of four Gaussian distributions. The shaded areas correspond to the contributions from different particle species.

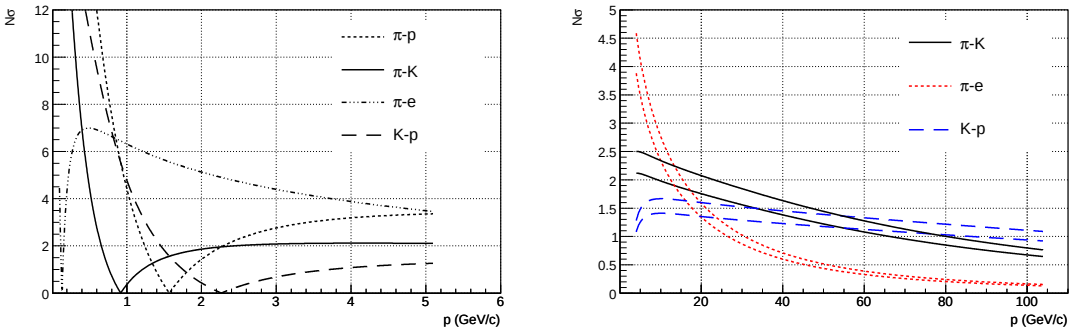

Figure 8.15: Momentum dependence of the $\langle \mathrm{d}E/\mathrm{d}x \rangle$ separation for different particle combinations in units of the energy loss resolution. Left: In the low-momentum range assuming a constant resolution of 6.5%. Right: In a wide momentum range, for a resolution of 5.5% (upper curves) and 6.5% (lower curves).

for a narrow momentum bin around $0.5\,\mathrm{GeV}/c$. The separation power (expressed as number of standard deviations) for the different pairs of particle species is plotted as a function of momentum in figure 8.15. In the lower momentum range (left panel), one starts with excellent separations in the $1/\beta^2$ region (below the particle masses). Increasing the momentum, the separations progressively worsen, decreasing to zero, at the value of momentum where the Bethe-Bloch curves for the two particles cross. At still higher momenta, the particle separation increases again thanks to the relativistic rise of the $\mathrm{d}E/\mathrm{d}x$ in the TPC gas, up to the Fermi plateau, before a final gentle decrease towards very high momenta. It is actually possible to measure separately the average abundances of the different particle species up to several tens of GeV of momentum, as can be seen from the right panel of figure 8.15.

The measurement of $\mathrm{d}E/\mathrm{d}x$ in the TRD contributes to charged-particle PID in the same momentum range as for the TPC. Although the ionization in the TRD gas (based on xenon) is larger than in the TPC (based on neon), the TRD $\mathrm{d}E/\mathrm{d}x$ measurement is only a complement to the TPC measurement, because of the limited TRD track length (the resolution scales as $\sqrt{L}$). The precision on the $\mathrm{d}E/\mathrm{d}x$ measurement in the TRD is estimated to be 18–20%.

2008 JINST 3 S08002

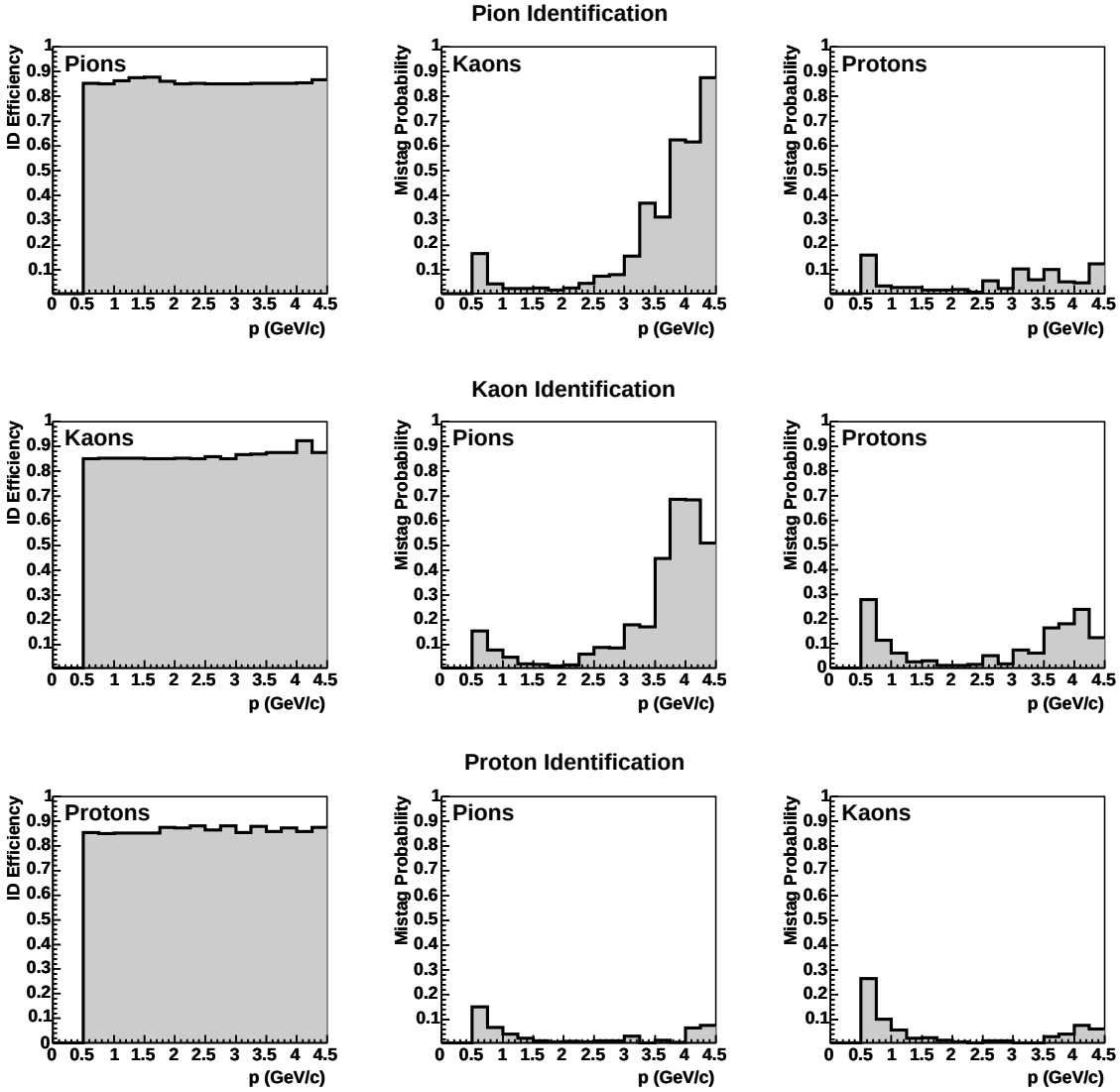

Figure 8.16: PID efficiencies (tuned at about 85%, see text) and mistag probabilities in the TOF for the case of pion (top), kaon (middle) and proton identification (bottom), for pions, kaons and protons in central Pb-Pb collisions.

As we also saw above, charged-particle identification based on a $\mathrm{d}E/\mathrm{d}x$ measurement performs well in the $1/\beta^2$ region and, for gas-based detectors, in the multi-GeV region. However, this technique inevitably leaves a hole in the momentum range around the minimum of the ionizing losses (i.e. between 0.9 and 3 GeV/c, see figure 8.15). In the ALICE experiment this range is covered by the TOF detector, that is able to measure a particle's arrival time with a precision of about 80 ps. During the last tracking pass in the Kalman filter we compute the integral of the particle's time-of-flight for different mass hypotheses, and compare it with the TOF measurement smeared by the response function. In this way, we obtain the TOF track probabilities for the different particle species. Figure 8.16 shows, for the central Pb-Pb collisions, the efficiency-contamination matrix for pion, kaon, and proton identification by the TOF, obtained tuning the correct-particle-identification

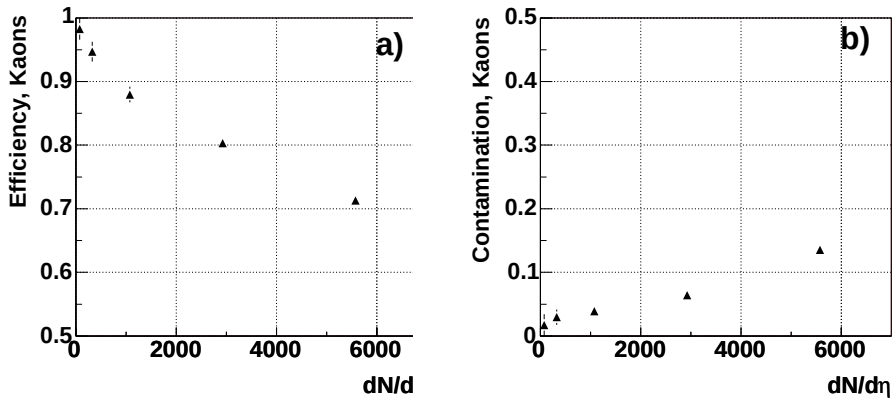

Figure 8.17: TOF PID efficiency (a) and contamination (b) for kaons, integrated over the momentum interval $0.5 < p < 3$ GeV/c, as a function of the charged-track multiplicity per unit rapidity.

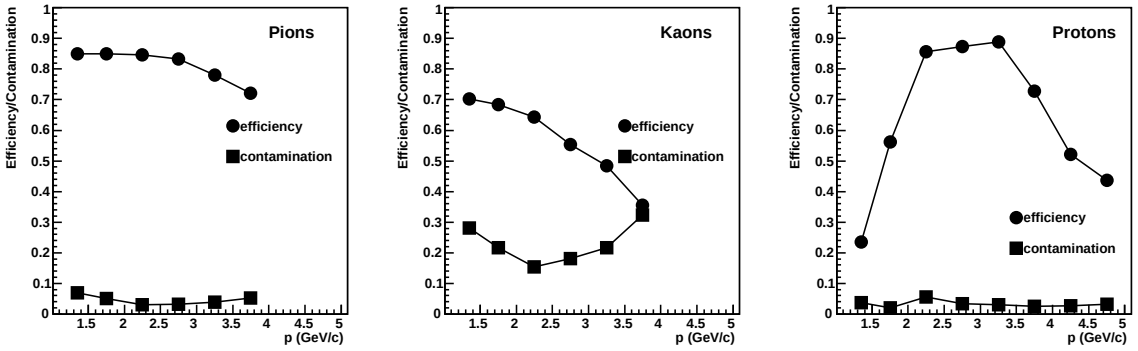

Figure 8.18: Efficiency and contamination for pions, kaons, and protons in the HMPID.

probability $\approx$ 85%. The TOF detector allows us to extend, on a track-by-track basis, the kaon/pion separation out to 2.5–3 GeV/c and the proton/kaon separation out to 3.5–4 GeV/c. The dependence of the TOF performance on the charged-particle density is shown in figure 8.17 for kaons.

The HMPID is used to further extend the momentum range for charged-particle identification, albeit only within a limited acceptance. The expected performance is shown in figure 8.18, where the momentum dependence of the identification efficiency and the contamination probability are plotted for different particle species. As can be seen, the HMPID is able to identify protons up to 5 GeV/c.

The various PID measurements are translated into probabilities for each track to belong to the different particle types. At the level of the measurements from the individual detectors, we do not attempt to take into account the differences in the different particle-species populations (as they will in general be different for each analysis, due to the different applied selection cuts). Such 'a priori' probabilities are taken into account at the combined PID stage (i.e. after the analysis cuts have been applied), using an iterative procedure. Simulation studies have shown that such a procedure converges to the correct values of the particle yields, in at most three iterations, even when starting with equal a priori probabilities for all particles. The combined particle identification performance of the ITS, TPC and TOF is shown, for the example of kaons in figure 8.19.

2008 JINST 3 S08002

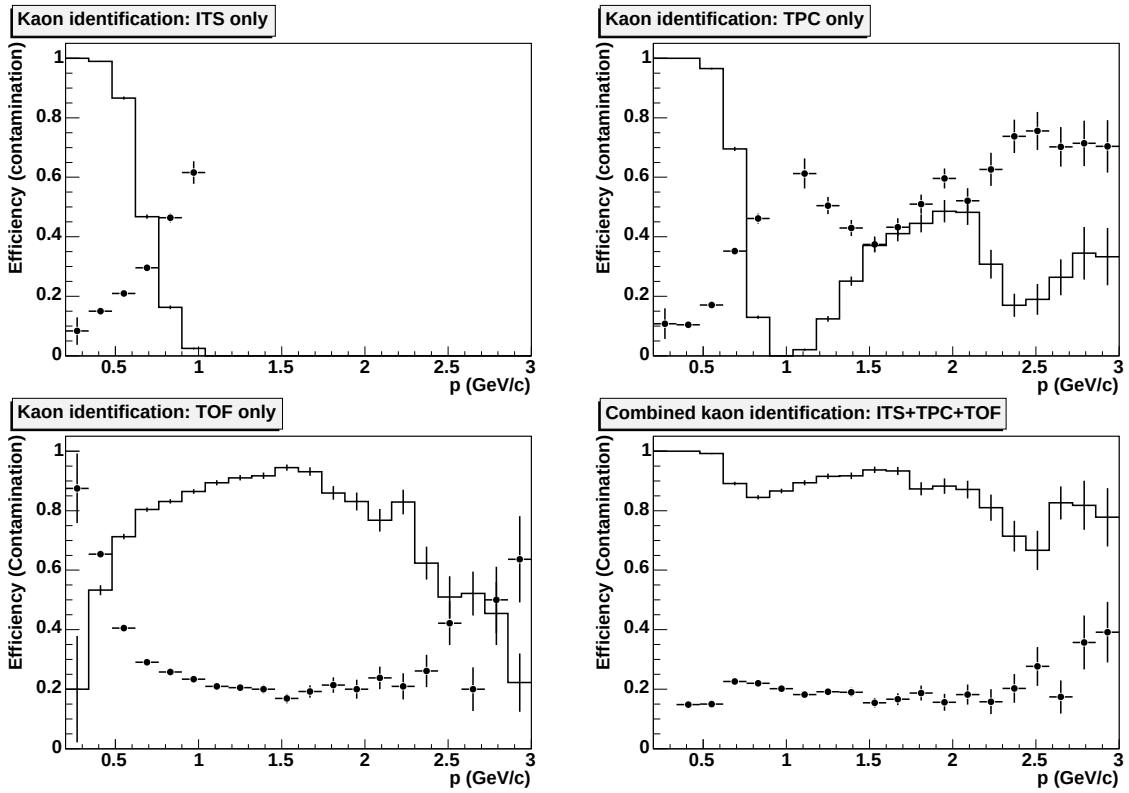

Figure 8.19: Single-detector efficiencies (solid line) and contaminations (points with error bars) for charged-kaon identification with the ITS, TPC and TOF stand-alone and combined.

8.2.2 Electron identification

The main source of information for electron identification in ALICE is the TRD (Transition-Radiation Detector), which can also provide electron-identification information at the trigger level. The TRD is expected to reject pions by a factor of 100 or better, for 90% electron detection efficiency. This is shown in figure 8.20 for particle momentum of 2 GeV/c. The charged-hadron rejection power is expected to deteriorate only very slowly as the momentum increases, making it possible to discriminate between pions and electrons up to a few tens of GeV. Figure 3.44 in section 3.3 shows an analysis of the pion rejection power as a function of the momentum employing different methods for particle identification. At low momenta the TPC also contributes to electron identification via the $\mathrm{d}E/\mathrm{d}x$ measurement (cf. figure 8.14).

Additional electron-identification capability, in particular at high momenta, will be provided by the ALICE electromagnetic calorimeters: the PHOS, in a restricted acceptance; and later the EMCal, expected to provide another two orders of magnitude of hadron rejection power.

8.3 Neutral-particle detection

Excellent photon-detection capability is provided by the PHOS. The expected energy resolution is shown in figure 8.21 as a function of energy. In order to extract the signal from the direct photons

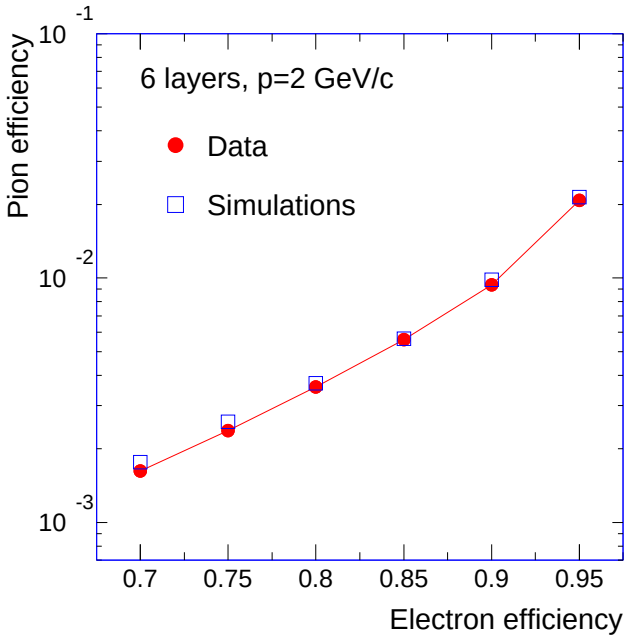

Figure 8.20: Pion efficiency as a function of electron efficiency in the TRD for a momentum of 2 GeV/c. Simulations are compared to data measured in test beams.

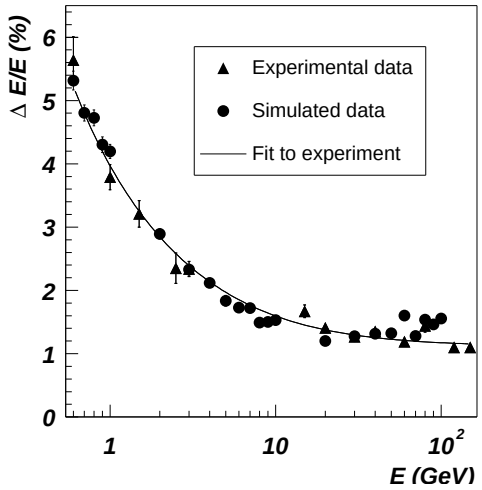

Figure 8.21: Energy resolution of a 3×3 $PbWO_4$ array measured in response to mono-energetic electrons (▲) compared with simulations of mono-energetic photons (●). The continuous line represents the result of the fit to the experimental data.

produced in heavy-ion collisions, it is necessary to measure the production of π^0, η, and other resonances in as wide a transverse-momentum range as possible. In figure 8.22 the performance of PHOS for the extraction of the π^0 signal is shown in bins of increasing p_t. The measured yields of π^0, η, etc. will then be used to subtract from the observed γ transverse momentum spectrum the contribution due to particle decays.

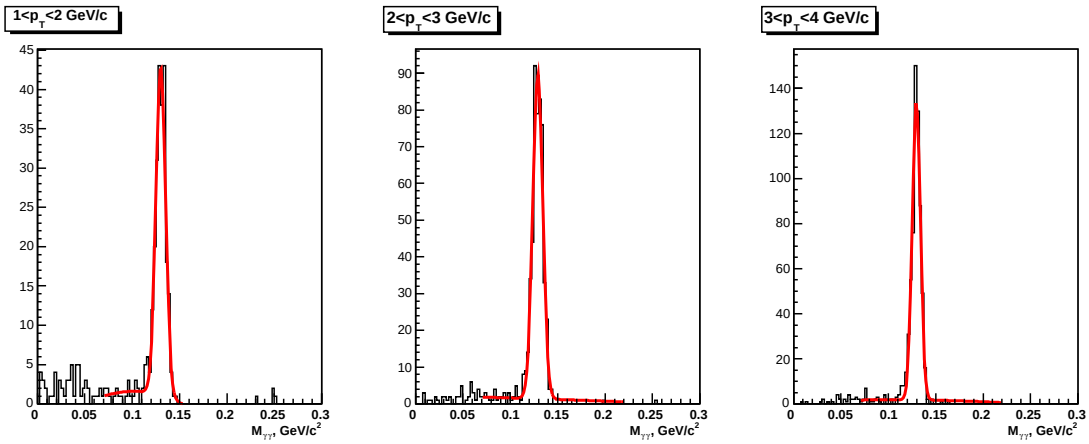

Figure 8.22: $\gamma\gamma$ invariant-mass spectra for different p_{t} bins.

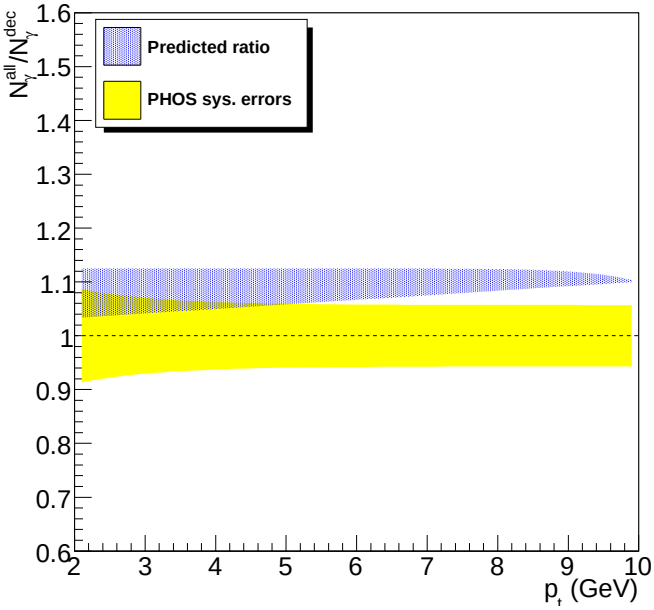

Figure 8.23: Error band, including systematic uncertainties, for the ratio of all photons to decay photons as a function of p_{t}.

In figure 8.23 the estimated error band, including systematic uncertainties, for the ratio of all photons to decay photons is shown. The excess above unity represents the direct photon signal. Above 10 GeV this signal is dominated by the production of QCD photons, which is expected to be well described by perturbative QCD calculations. In the few GeV region additional photon radiation from the initial high-density phase of the heavy-ion collisions is expected. As illustrated in figure 8.23, such a signal should be observable, if it amounts to at least 6% of the contribution from π^0, η, etc. decays.

Additional capabilities for the detection of neutral particles will be provided by the EMCal detector over a larger acceptance, but with lower energy resolution (by a factor 2.5–3) than PHOS.

2008 JINST 3 S08002

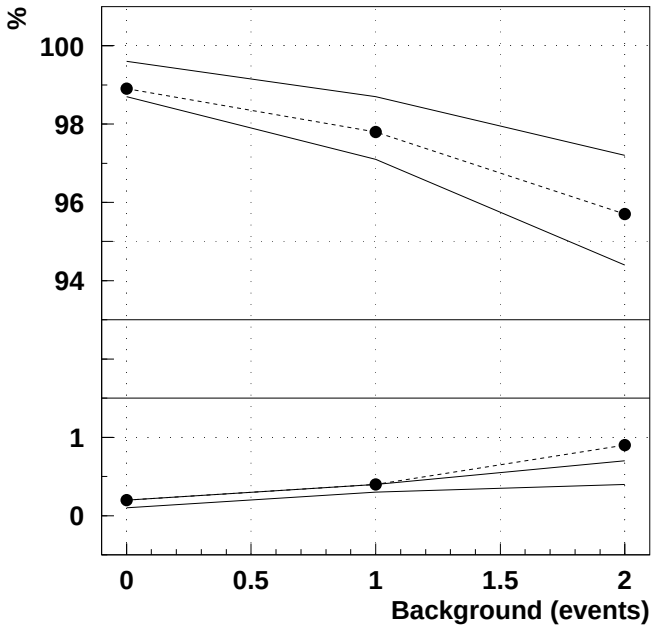

Figure 8.24: Track-finding efficiency (upper part) and percentage of fake tracks (lower part) versus occupancy, expressed in terms of the number of superimposed nominal background events. The closed points show results of the tracklet matching method. The bands show the results for the Kalman filter for different algorithm parameters. Lines are drawn to guide the eye.

The EMCal will also open the possibility of triggering on high-transverse-momentum jets and will allow us to improve the measurement of the jet energy including the neutral component. Finally, another photon detector, the PMD, will allow us to count the number of photons produced in the forward region ($2.5 < \eta < 3.5$).

8.4 Muon detection

Muons are detected in the muon spectrometer in the pseudo-rapidity range $-4.0 < \eta < -2.5$. The muon tracks are reconstructed by five tracking stations located behind the absorber. The measurement of their deflection in the muon dipole magnet allows the determination of their momenta. Two different methods have been developed for track finding in the spectrometer. The first combines tracklets found in the muon tracking stations (each station measures two space points on the track); the second is based on the Kalman filter. The two methods give compatible results. A comparison of the two methods is shown in figure 8.24; the muon-finding efficiency and the fake-track probability are shown as a function of the background level in the tracking stations, expressed in terms of number of superimposed central Pb-Pb events. A tracking efficiency above 95% is obtained, even at a level of background twice that expected in central Pb-Pb collisions.

The momentum resolution for the reconstructed tracks is shown in figure 8.25 as a function of momentum. We achieve a relative momentum precision of about 1%, which then results in a contribution to the invariant-mass resolution for dimuons of about 0.7% ($(1/\sqrt{2} \times \Delta p/p)$. The remaining contribution to the dimuon invariant-mass resolution, due to the error on the determination of the

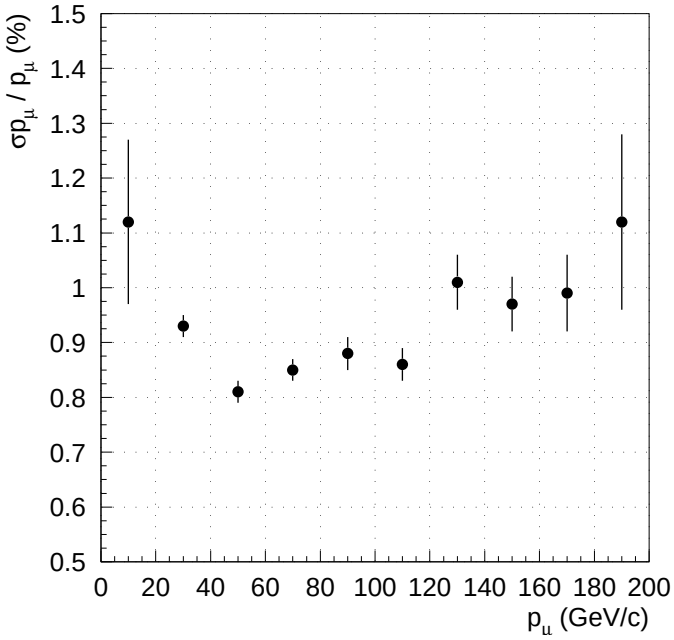

Figure 8.25: Relative momentum resolution as a function of momentum for muons from Υ decays.

angle between the two muons, is lower. This is due to the fact that the primary-vertex constraint is used in the muon reconstruction, which allows to determine the angle using the positions of the primary-vertex and of the first measured point behind the absorber, and not by just relying on the measured track direction in the tracking stations. The precision on the angle is therefore determined essentially by the resolution on the first measured point. As a consequence, the mass resolution for the Υ reconstruction is better than $100\,\mathrm{MeV}/c^2$, which allows for unambiguous separation of the different Υ states.